ADVANCED FUNCTIONAL MATERIALS
www.afm-journal.de

2D Phosphorene-Decorated Ni-Rich Layered Cathodes for High-Power and High-Energy Li-Ion Batteries

Jihoe Lee, Kijeong Nam, Bonyoung Ku, Myungeun Choi, Min-kyung Cho, Su Yeon Jung, Jinhong Min, Jinho Ahn, Yongseok Lee, Sang-Yeop Lee, Dohyun Lee, Yun Seong Cho, Da-Sol Kwon, Jung-Keun Yoo, Joohoon Kang, and Jongsoon Kim**

To meet the demands of high-energy lithium-ion batteries (LIBs), cathodes must achieve high mass loading and low carbon content without compromising rate capability or cycling stability. However, the intrinsically low electronic conductivity of conventional surface coatings limits their effectiveness under high mass loading and low carbon content conditions. Here, a surface modification strategy leveraging conductive and chemically stable 2D phosphorene (2DP), electrochemically exfoliated from black phosphorus, is presented to modify the surface of $Li[Ni_{0.8}Co_{0.1}Mn_{0.1}]O_2$ (NCM811) cathodes. The 2DP-decorated NCM811 (2DP-NCM811) delivers a high discharge capacity of 209.7 mAh g^{-1} at 30 mA g^{-1} and maintains 183.2 mAh g^{-1} at 500 mA g^{-1} under practical conditions (18 mg cm^{-2} cathode loading, 1 wt.% carbon). Compared to bare and phosphate-decorated counterparts, 2DP-NCM811 exhibits enhanced power capability. It also shows improved cycling stability with 82.7% capacity retention after 100 cycles, outperforming bare NCM811 (73.8%) and phosphate-decorated NCM811 (80.1%). *Operando* X-ray diffraction and ex situ transmission electron microscopy confirm that the application of 2DP effectively suppresses structural degradation. This study demonstrates a surface engineering strategy that addresses both structural instability and electronic limitations by integrating a conductive and chemically stable 2D material, offering a scalable route toward high-performance LIB cathodes.

1. Introduction

Global concerns over climate change and carbon emissions have intensified the demand for sustainable energy storage systems, particularly for transportation and grid-scale applications.[1,2] As a result, the application of Li-ion batteries (LIBs) has expanded beyond small electronic devices like mobile phones to large-scale applications such as electric vehicles (EVs).[3–5] This expansion has led to a global surge in interest and demand for LIBs, driving extensive research and development efforts to secure key technologies in this field.[6–8]

In particular, intensive research has been conducted to increase the energy density of cathodes as a means to enhance the overall energy density of LIBs.[9,10] It has been reported that high energy density can be achieved by increasing the Ni content in the layered oxide, $Li[TM]O_2$.[11,12] Thus, $Li[Ni_{0.8}Co_{0.1}Mn_{0.1}]O_2$ (NCM811), one of Ni-rich layered oxide cathodes, has received great attention as the promising cathode for LIBs, due to its reversible gravimetric capacity approaching ≈200 mAh g^{-1} and the average operation voltage of ≈3.7 V (vs Li^+/Li).[13–15]

However, in the case of the NCM811 cathode, Ni^{4+} ions formed during charging undergo an irreversible reaction through side reactions with the electrolyte, reducing to Ni^{2+}.[16] Due to the similar ionic radius of Li^+(0.76Å) and Ni^{2+}(0.69Å), Ni^{2+} ions are easily migrated into the Li-layer, leading to cation disorder.[17–19] After prolonged cycling, the surface of the NCM811 particles

---

J. Lee, B. Ku, M. Choi, J. Ahn, Y. Lee, S.-Y. Lee, J. Kim
Department of Energy Science
Sungkyunkwan University
Suwon 16419, Republic of Korea
E-mail: jongsoonkim@skku.edu

J. Lee, B. Ku, M. Choi, J. Ahn, Y. Lee, S.-Y. Lee, J. Kim
SKKU Institute of Energy Science and Technology (SIEST)
Sungkyunkwan University
Suwon 16419, Republic of Korea

The ORCID identification number(s) for the author(s) of this article can be found under https://doi.org/10.1002/adfm.202511385

DOI: 10.1002/adfm.202511385

K. Nam, S. Y. Jung, D. Lee, Y. S. Cho
School of Advanced Materials Science and Engineering
Sungkyunkwan University
Suwon 16419, Republic of Korea

K. Nam, J. Min, J. Kang
Department of Chemical and Biomolecular Engineering
Yonsei University
Seoul 03722, Republic of Korea
E-mail: joohoon@yonsei.ac.kr

M.-kyung Cho
Advanced Analysis Center
Korea Institute of Science and Technology (KIST)
Seoul 02792, Republic of Korea

D.-S. Kwon, J.-K. Yoo
Energy Storage Research Center
Korea Institute of Science and Technology (KIST)
Seoul 02792, Republic of Korea

converts through a spinel-like compound and ultimately forms an electrically insulating rocksalt-type NiO.[20,21] This undesirable surface degradation significantly deteriorates the electrochemical properties of the NCM811 cathode, including power capability and cyclability.

To prevent surface degradation, various oxide-based and polyanion-based coatings such as Al_2O_3, ZrO_2, Li_2O-$2B_2O_3$, and PO_4 have been applied to NCM811 particles.[22–25] While these coatings enhance structural stability, their intrinsically low electronic conductivity impairs electron transport within the electrode. This issue becomes particularly critical in practical high-energy-density cell configurations, where the amount of conductive carbon is minimized to maximize the active material fraction.[26,27] In particular, under high mass loading conditions required for practical electrodes, the limited electron transport through oxide coatings can lead to severe polarization and sluggish reaction kinetics, ultimately degrading rate capability. Therefore, alternative coating materials with higher conductivity and strong chemical and mechanical stability are required. In addition, a method for forming thin and uniform coatings that do not compromise the electrochemical activity is essential.

In this study, we introduce 2D phosphorene nanosheets (2DP), electrochemically exfoliated from black phosphorus, as a high-conductivity surface modifier for NCM811 cathodes.[28,29] 2DP has a unique puckered structure, which provides exceptional mechanical flexibility and allows the nanosheets to conform tightly to the curved surfaces of NCM811 particles.[30,31] This ensures intimate interfacial contact, thereby enhancing both electronic conductivity and structural stability. In addition, 2DP offers high carrier mobility, enabling efficient and stable electron conductivity compared to metallic or insulating coatings.[32,33] Beyond its electronic and structural advantages, 2DP forms uniform and conformal coverage on NCM811 surfaces, minimizing interfacial voids and reducing contact resistance, thereby enhancing interfacial compatibility. These features make 2DP a compelling candidate for suppressing surface reactions and stabilizing interfacial structure under practical cycling conditions.

The resulting 2DP-decorated NCM811 (2DP-NCM811) was prepared by incorporating 2DP with ethyl cellulose (EC), which served to improve interfacial adhesion and promote a uniform coating morphology. This combination established continuous conductive pathways within the electrode and contributed to the enhanced electrochemical performance. Under high mass loading (18 mg cm^{-2}) and low conductive carbon content (1 wt.%), 2DP-NCM811 delivered a high discharge capacity of 209.7 mAh g^{-1} at a current density of 30 mA g^{-1}, outperforming bare NCM811 (B-NCM811, 192.63 mAh g^{-1}) and phosphate-decorated NCM811 (PO-NCM811, 179.86 mAh g^{-1}). Even at a high current density of 500 mA g^{-1}, 2DP-NCM811 retained a specific capacity of 183.2 mAh g^{-1}, while B-NCM811 and PO-NCM811 showed only 161.9 and 160.1 mAh g^{-1}, respectively. In addition, 2DP-NCM811 exhibited improved cycling retention of 82.7% after 100 cycles, significantly higher than B-NCM811 (73.8%) and PO-NCM811 (80.1%).

Operando X-ray diffraction (XRD) and ex situ transmission electron microscopy (TEM) analyses confirmed the suppressed structural degradation in 2DP-NCM811. These results demonstrate that this 2D phosphorene-based modification strategy offers a viable route toward high-performance and durable LIB cathodes. Unlike conventional oxide coatings, this approach uniquely combines high electronic conductivity, mechanical conformity, and interfacial stability. This work presents a new direction for designing cathode surfaces under practical electrode conditions.

2. Results and Discussion

2.1. Preparation of 2D Phosphorene Nanosheets (2DP)-Decorated NCM811 Cathode (2DP-NCM811)

Figure 1a shows a schematic illustration of molecular intercalation driven electrochemical exfoliation of 2DP in solution and wrapping on NCM811 to prepare 2DP-NCM811.[33] Molecular intercalation driven electrochemical exfoliation is a method to prepare atomically-thin 2D nanosheets in large quantities using a molecular intercalant under the electrochemical potential application.

During the process, tetrabutylammonium ions (TBA^+) were intercalated into the van der Waals gaps of layered BP crystals, causing the volume expansion due to increased inter-layer distance. This process results in the van der Waals interaction weakening, so that 2DP are easily exfoliated under mild sonication in *N*,*N*-dimethylformamide (DMF). This dispersion was centrifuged repeatedly to obtain a few-layer 2DP by discarding non-exfoliated BP. From 50 mg of bulk BP, this process typically yielded ≈3 mL of 2DP dispersion at 0.68 mg mL^{-1}, corresponding to a yield of ≈4% and productivity of ≈1 mg h^{-1} (Table S1, Supporting Information).

Furthermore, DMF was changed to low-boiling-point isopropyl alcohol (IPA) to minimize residual solvents after the process. Due to the ambient instability of 2DP, the entire process was carefully done in an Ar-sealed chamber, and anhydrous solvents were utilized (more details are in the experimental section).[34–36] Subsequently, the NCM811 powders were introduced into the 2DP solution, followed by mild sonication to promote uniform wrapping of the 2DP onto the surface of the NCM811 particles.

After ensuring homogeneous dispersion, the mixture was subjected to evaporation to remove the IPA solvent. Finally, the resulting composite was calcined under an Ar atmosphere for a short duration in order to minimize the oxidation of 2DP during the thermal treatment. This systematic coating procedure allowed for the formation of a uniform and thin 2DP layer on the surface of NCM811, effectively contributing to improved structural stability and enhanced both ionic and electronic conductivity.

Following the 2DP preparation, the exfoliated 2DP were characterized with a comprehensive suite of microscopic and spectroscopic analyses. In Figure 1b, the atomic force microscopy (AFM) images show the representative structures of exfoliated 2DP. As shown in Figure 1c,d, the thickness of the exfoliated 2DP has a distribution between 2 and 12 nm, with the majority of the 2–3 nm samples, corresponding to 3–5 layers of 2DP.[37] The lateral size of 2DP shows an average value of 0.53 µm. Additionally, the batch-to-batch uniformity of lateral size and thickness was confirmed through AFM measurements of independently synthesized samples, as shown in Figure S1 (Supporting Information).

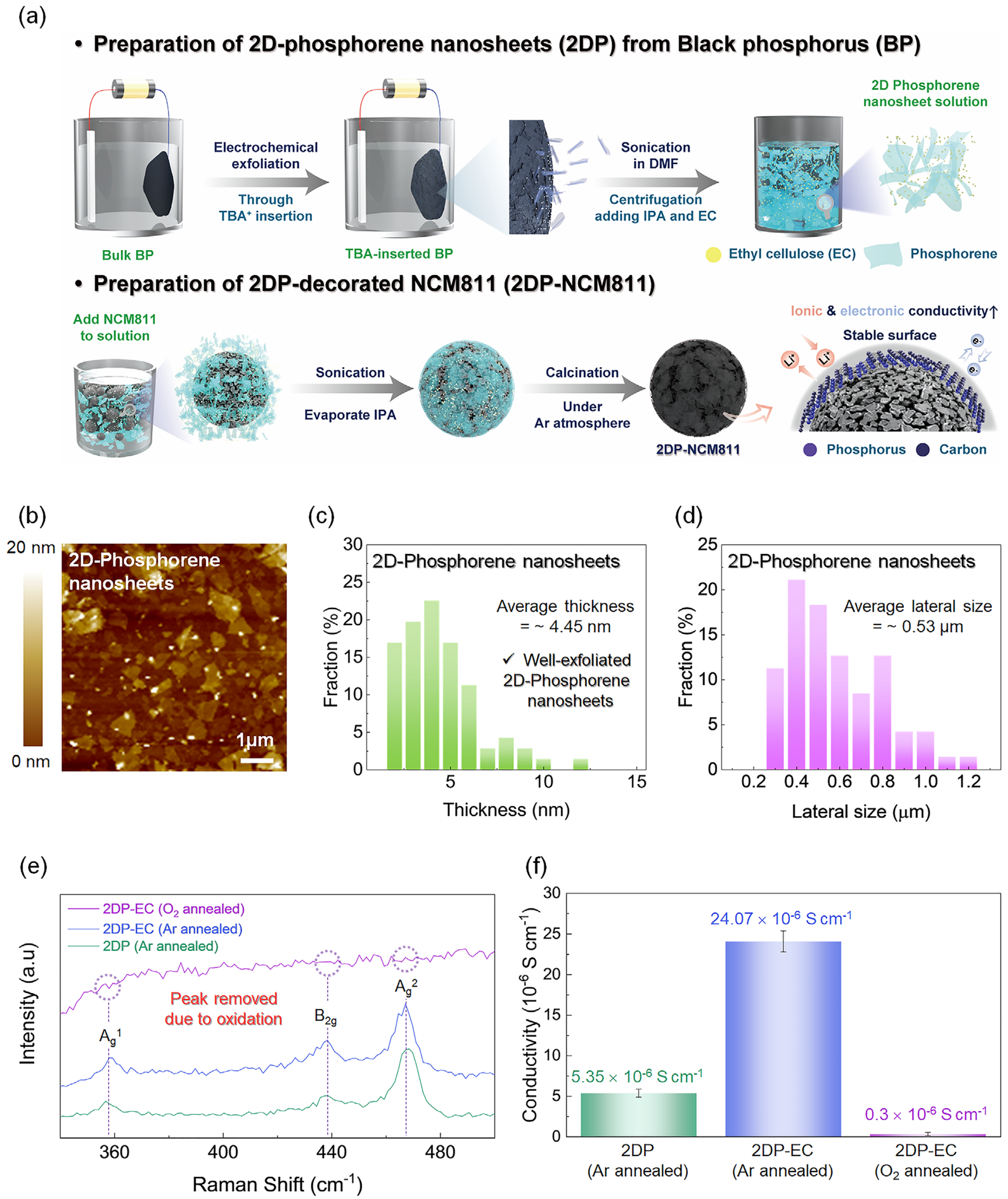

Figure 1. a) Schematic illustration of the preparation processes of 2DP and 2DP-NCM811 with the advantages of the 2DP-decorated coating on NCM811. b) AFM analysis of 2DP flakes. c) Thickness and d) lateral size of 2DP. e) Comparison of Raman spectra of 2DP-EC mixture according to the calcination condition. f) Conductivity of the bare 2DP and 2DP-EC film according to the condition of calcination, with error bars.

This structural uniqueness of 2D nanosheets enables wrapping NCM811 particles in a uniform and conformal manner with effective van der Waals interface formation.[38,39] The crystallinity of 2DP after electrochemical exfoliation was characterized by Raman spectroscopy shown in Figure S2 (Supporting Information). The representative Raman modes of 2DP, including A_g^1, B_{2g}, and A_g^2 peaks, are clearly shown at ≈358, 438, and 467 cm^{-1}, respectively. Also, high A_g^2–A_g^1 ratio of Raman intensity indicates the atomically-thin structure in the thickness of the exfoliated 2DP.[40]

Following the 2DP preparation and characterization, ethyl cellulose (EC) was added to the dispersion to form a conductive pathway between 2DP and NCM811 by thermally converting into a carbon interfacial layer. To determine the optimal ratio between 2DP and EC, we prepared cathodes by coating NCM811 active materials with various 2DP and EC ratios using a low loading of 2 mg cm^{-2} and a carbon source content of 5 wt.%, followed by cycling tests (Figure S3, Supporting Information).

The cathode coated with a solution without EC exhibited discharge capacity and retention performances similar to those of B-NCM811. Meanwhile, the cathode coated with a solution containing 2DP and EC in a 1:2 ratio showed relatively high retention but significantly low discharge capacity. In contrast, the cathode prepared using a solution with a 1:1 2DP-to-EC ratio demonstrated superior electrochemical performance, achieving a high retention of 93.43% and a discharge capacity of 188.27 mAh g^{-1} after 70 cycles. Based on these results, we identified the optimal 2DP:EC ratio as 1:1 and proceeded with subsequent experiments accordingly.

In addition, we investigated the property changes in the mixture of 2DP-EC according to the heat treatment conditions. As shown in Figure 1e, the Raman peaks of 2DP after various thermal processes are shown, respectively. When the 2DP-EC mixture was annealed in an O_2 atmosphere, the peaks were removed due to oxidation. Oxidation of phosphorene to phosphate, composed of P—O bonding, lost its intrinsic properties, and its electronic performance will be degraded contrast to that of 2DP. On the other hand, when the 2DP-EC mixture was calcinated in an Ar atmosphere, the peaks were well retained.

Moreover, as shown in Figure 1f, we compared electrical conductivities of the 2DP-EC mixtures after heat treatment under Ar and O_2 atmospheres, respectively, through current-voltage measurements (Figure S4, Supporting Information). It was verified that the conductivity of the 2DP-EC mixture annealed under an Ar atmosphere is ≈24.07×10^{-6} S cm^{-1}, which is much higher than that of both the 2DP-EC mixture annealed under an O_2 atmosphere (≈0.3×10^{-6} S cm^{-1}) and bare 2DP annealed under an Ar atmosphere (≈5.35×10^{-6} S cm^{-1}). These results imply that the heat treatment of a 2DP-EC mixture under an Ar atmosphere facilitates the optimum preparation of 2DP-NCM811, offering enhanced electrochemical performances through simultaneous improvements in structural stability and electrical conductivity.

2.2. Structure and Morphology of 2D Phosphorene Nanosheets (2DP)-Decorated NCM811 Cathode (2DP-NCM811)

To verify the successful preparation of 2DP-NCM811, we performed XRD measurement and Rietveld refinement. As shown in **Figure 2a**, 2DP-NCM811 exhibits a hexagonal-based layered structure with $R\bar{3}m$ symmetry. The detailed structural information on 2DP-NCM811, such as the atomic coordinates, thermal factor (B_{iso}), and occupancies, is tabulated in Table S2 (Supporting Information). The reliability factor of 2DP-NCM811 (R_p = 7.83%, R_I = 9.32%, R_F = 1.93%, χ^2 = 1.89%) proved the high accuracy of the refinement.

In addition, we compared the XRD patterns of 2DP-NCM811, bare NCM811 (B-NCM811), and NCM811 with phosphate (P—O bonding)-decorated coating (PO-NCM811). It was confirmed that the three samples have the same crystal structure (Figure S5, Supporting Information). These results indicate that the crystal structure of NCM811 was well retained after the 2DP-decorated coating process.

To investigate the 2DP-decorated coating on NCM811 particles, we performed high-resolution transmission electron microscopy (HRTEM) analyses. The B-NCM811 particle just shows the smooth surface without a coating layer (Figure S6, Supporting Information). In the case of the PO-NCM811 particle, its coating layer has a thickness ranging from 5 to 10 nm, formed unevenly and relatively thick, which is expected to hinder Li^+ diffusion during charge–discharge. On the other hand, 2DP-NCM811 particles have a uniform and thin coating layer with a thickness of just 1.5 nm (Figure 2b). Moreover, the fast Fourier transform (FFT) analyses of the HRTEM images confirmed an interplanar spacing of ≈0.243 nm, consistent with the characteristic d-spacing of the (101) plane in the NCM811 structure. To further validate the coating conformity of the 2DP layer, we analyzed additional TEM images collected from multiple 2DP-NCM811 particles. As shown in Figure S7 (Supporting Information), the HRTEM images and histogram compiled from the independent regions confirm that the coating thickness is narrowly distributed ≈1.5 nm, indicating a highly uniform and conformal coating.

Through scanning electron microscopy (SEM) analysis, it was also verified that 2DP-NCM811 has similar particle morphology and size (≈5 μm) to B-NCM811, while displaying surface differences caused by the 2DP-decorated coating (Figure 2c,d). These results imply that the uniform and thin 2DP-decorated coating with carbon in 2DP-NCM811 can suppress the side reactions and provide the electrically conductive pathways during charge–discharge, thereby enhancing the electrochemical performances compared to both PO-NCM811 and B-NCM811.

The 2DP-decorated coating in 2DP-NCM811 was also confirmed through the SEM based energy dispersive X-ray spectroscopy (EDS) elemental mapping analyses. As shown in Figure 2e, it was verified that not only Ni, Co, and Mn but also P and C elements are homogenously distributed in the secondary particle of 2DP-NCM811.

In addition, Raman spectroscopy was employed to further investigate the P—C and P—P bonds in 2DP-NCM811. As shown in Figure 2f, in the Raman data of 2DP-NCM811, P—P and P—C bonds were detected in the range of 300–500 cm^{-1} and 650–770 cm^{-1}, respectively.[41] The D and G bands attributed to the conductive carbon in the 2DP-NCM811 electrode were also observed at ≈1320 and 1580 cm^{-1}, respectively. These results clearly indicate that the 2DP-decorated coating with carbon on NCM811 particles in 2DP-NCM811 was successfully achieved. In terms of B-NCM811 and PO-NCM811, no signals on P—P and P—C bonds

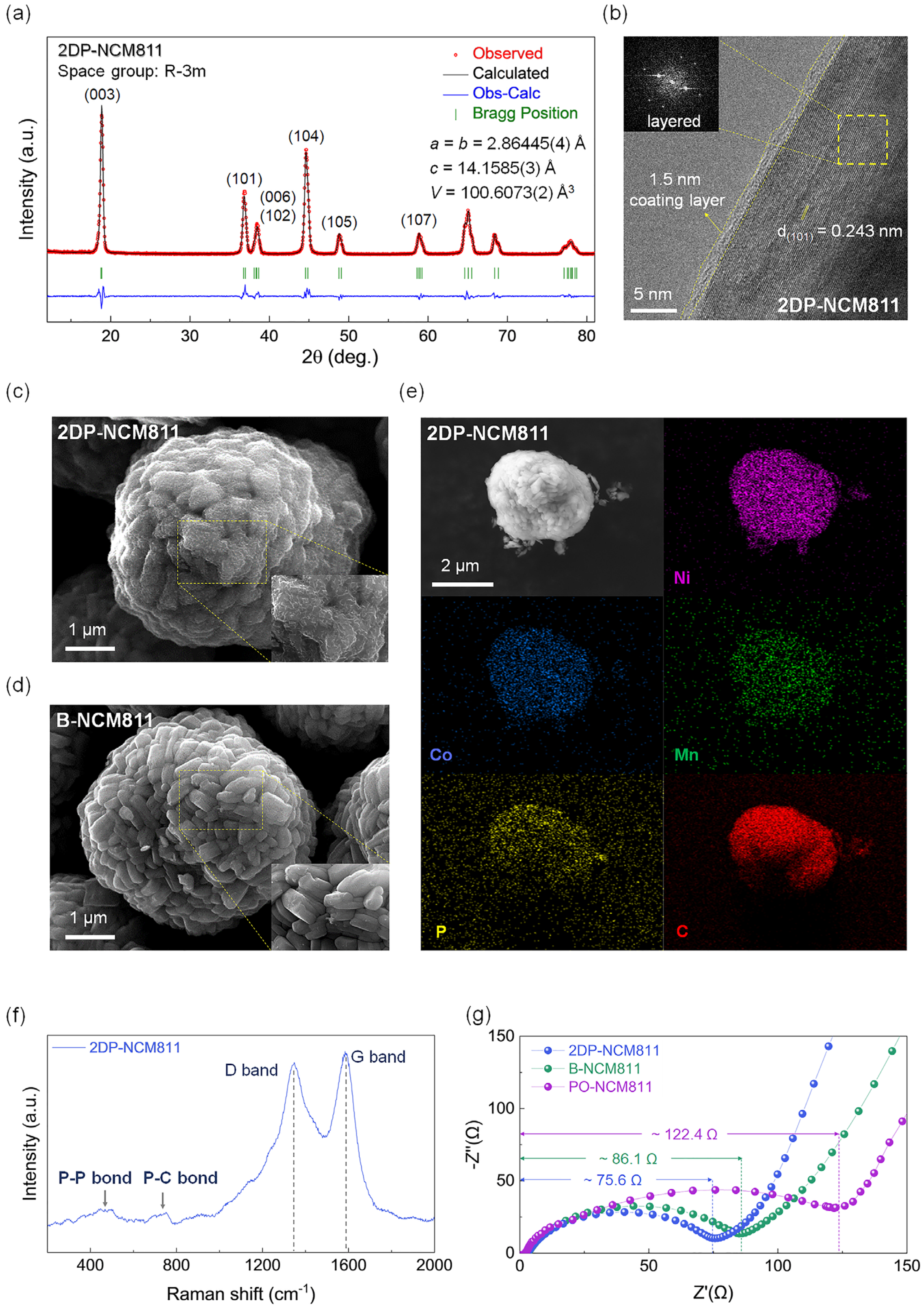

Figure 2. a) Rietveld refinement of the XRD pattern of 2DP-NCM811. b) HRTEM image of 2DP-NCM811 and corresponding FFT image. SEM images of c) 2DP-NCM811 and d) B-NCM811. e) SEM-EDS mapping images of 2DP-NCM811. f) Raman spectra of the 2DP-NCM811 cathode. g) EIS results of the electrodes after 1 activation cycle.

cannot be detected in their Raman data (Figure S8, Supporting Information).

To deepen our comprehension of the improved conductivity exhibited by the 2DP-decorated coating with carbon, electrochemical impedance spectroscopy (EIS), as depicted in Figure 2g, was measured after one activation cycle.[42] The observed semicircle size for 2DP-NCM811, ≈75.6 Ω, was significantly smaller than the corresponding value observed for B-NCM811 and PO-NCM811, which measured ≈86.1 and ≈122.4 Ω. These results suggest that improved Li^+ diffusion kinetics by the 2DP-decorated coating with carbon enables the effective enhancement of the electrochemical performances of the NCM811 cathode, such as fast charge–discharge (Ch/Dis) performances and power capability. To further investigate the contribution of carbon coating alone, we additionally conducted an EIS test of EC-NCM811, which was fabricated by applying EC coating followed by identical thermal treatment. As shown in Figure S9 (Supporting Information), EC-NCM811 exhibited a reduced semi-circle size of ≈82.1 Ω, lower than that of B-NCM811 but still larger than 2DP-NCM811, indicating that the EC-derived carbon contributes partially to improved Li^+ diffusion kinetics.

2.3. Electrochemical Performances of 2D Phosphorene Nanosheets (2DP)-Decorated NCM811 Cathode (2DP-NCM811)

Figure 3a illustrates the comparison of electrochemical performances among 2DP-NCM811, B-NCM811, and PO-NCM811 in a half-cell system, tested at a current density of 30 mA g^{-1} within a voltage range of 3.0–4.3 V (vs Li/Li^+). All cathode electrodes were prepared with a mass loading of ≈18 mg cm^{-2} and ≈1% carbon content, reflecting the characteristics of low-carbon, high-loading electrodes. As measured from the cross-sectional SEM image of the electrode (Figure S10, Supporting Information), the thickness of the 2DP-NCM811 electrode was ≈59 µm. This falls within the practically relevant range for high-energy-density lithium-ion batteries.[43,44] Therefore, our electrode design is suitable for practical applications, ensuring the relevance of the observed performance improvements.

While discharge capacity of 2DP-NCM811 is ≈209.7 mAh g^{-1}, B-NCM811 and PO-NCM811 just delivered ≈192.62 and ≈179.86 mAh g^{-1}, respectively. In terms of Coulombic efficiency, 2DP-NCM811 achieved ≈98.66%, which is better than B-NCM811 (≈92.28%) and PO-NCM811 (≈87.88%). These results clearly show that 2DP-decorated coating can successfully enhance the electrochemical performance of the NCM811 cathode.

The enhanced electrical conductivity by 2DP-decorated coating is also confirmed through comparison of power capability (Figure 3b; Figure S11, Supporting Information). The corresponding error bars, obtained from triple determination, are provided in the Supporting Information (Figure S12, Supporting Information). Even at a high current density of 500 mA g^{-1}, 2DP-NCM811 exhibited a discharge capacity of ≈183.2 mAh g^{-1}, while the capacities of B-NCM811 and PO-NCM811 were just ≈161.9 and ≈160.12 mAh g^{-1} at the same conditions (Figure S13, Supporting Information). It was reported that at high current densities, the electrochemical performance of low-carbon, high-loading electrodes is hindered by limited Li^+ diffusion.[26,27] The 2DP-decorated coating enhances Li^+ diffusion, resulting in a significant increase in discharge capacity even at high current densities compared to B-NCM811 and PO-NCM811. Furthermore, to evaluate the independent impact of EC-derived carbon, EC-NCM811 was conducted under the same conditions (Figure S14, Supporting Information). Although EC-NCM811 showed improved capacity (≈165 mAh g^{-1} at 500 mA g^{-1}) compared to B-NCM811, 2DP-NCM811 maintained a significantly higher capacity at all current densities, clearly demonstrating superior conductivity attributed to 2DP-decorated coating.

Moreover, we compared the average discharge voltages of the three samples along the current density (Figure 3c). The difference in average discharge voltages among the cathodes becomes increasingly pronounced at higher discharge current densities. At 500 mA g^{-1}, the difference between 2DP-NCM811 and B-NCM811 reaches up to 0.07 V, while the difference between 2DP-NCM811 and PO-NCM811 is even larger, reaching up to 0.13 V.

Based on discharge voltage and capacity, both energy density and power density were calculated (Figure 3d). 2DP-NCM811 delivered outstanding performances in both discharge voltage and capacity, indicating the significant enhancement of fast Ch/Dis performance in 2DP-NCM811 compared to B-NCM811 and PO-NCM811.

The improvement in electrical conductivity plays a critical role in maintaining discharge voltage by minimizing resistive losses within the 2DP-NCM811 particles. This enhancement facilitates efficient charge transport and contributes to the overall stability of the particles during discharge.

Moreover, the 2DP-decorated coating can provide stable cycle-performance for the NCM811 cathode. To further verify the superior Li^+ diffusion of 2DP-NCM811, a galvanostatic intermittent titration technique (GITT) test was conducted for both 2DP-NCM811 and B-NCM811 (Figure 3e,f). The Li^+ diffusion coefficient (D_{Li^+}) from the GITT test was calculated using Equation (1).[45]

$$D_{Li^+} = \frac{4}{\pi\tau}\left(\frac{mV}{MS}\right)^2\left(\frac{\Delta E_s}{\Delta E_t}\right)^2, \quad \left(\tau \ll \frac{L^2}{D}\right) \tag{1}$$

In Equation (1), τ designates the time duration during the constant current, where m and M stand for the electrode's mass and the molar mass of the electrode. V stands for the molar volume of the electrode, S signifies the active surface area of the electrodes, and ΔE_s and ΔE_t represent the voltage change during a single step and the cumulative voltage change under GITT test conditions.

Consistent with the power capability results, 2DP-NCM811 exhibited an average diffusion coefficient of 1.09×10^{-7} cm^2 s^{-1}, during charge–discharge, which is higher than the diffusion coefficient of 0.57×10^{-7} cm^2 s^{-1} observed for B-NCM811, confirming its enhanced Li^+ diffusivity.

As shown in Figure 3g, we compared the cyclability of 2DP-NCM811, B-NCM811, and PO-NCM811 under the half-cell system. It was revealed that the 2DP-NCM811 cathode exhibited enhanced capacity retention of ≈82.65% after 100 cycles at 200 mA g^{-1}, while the capacity retention of B-NCM811 and PO-NCM811 was observed to be just ≈73.76% and ≈80.14%, respectively. Additionally, we compared the cyclability of the cathodes under two conditions: elevated temperature (45 °C) and higher cutoff voltage (4.5 V) (Figure S15, Supporting Information).

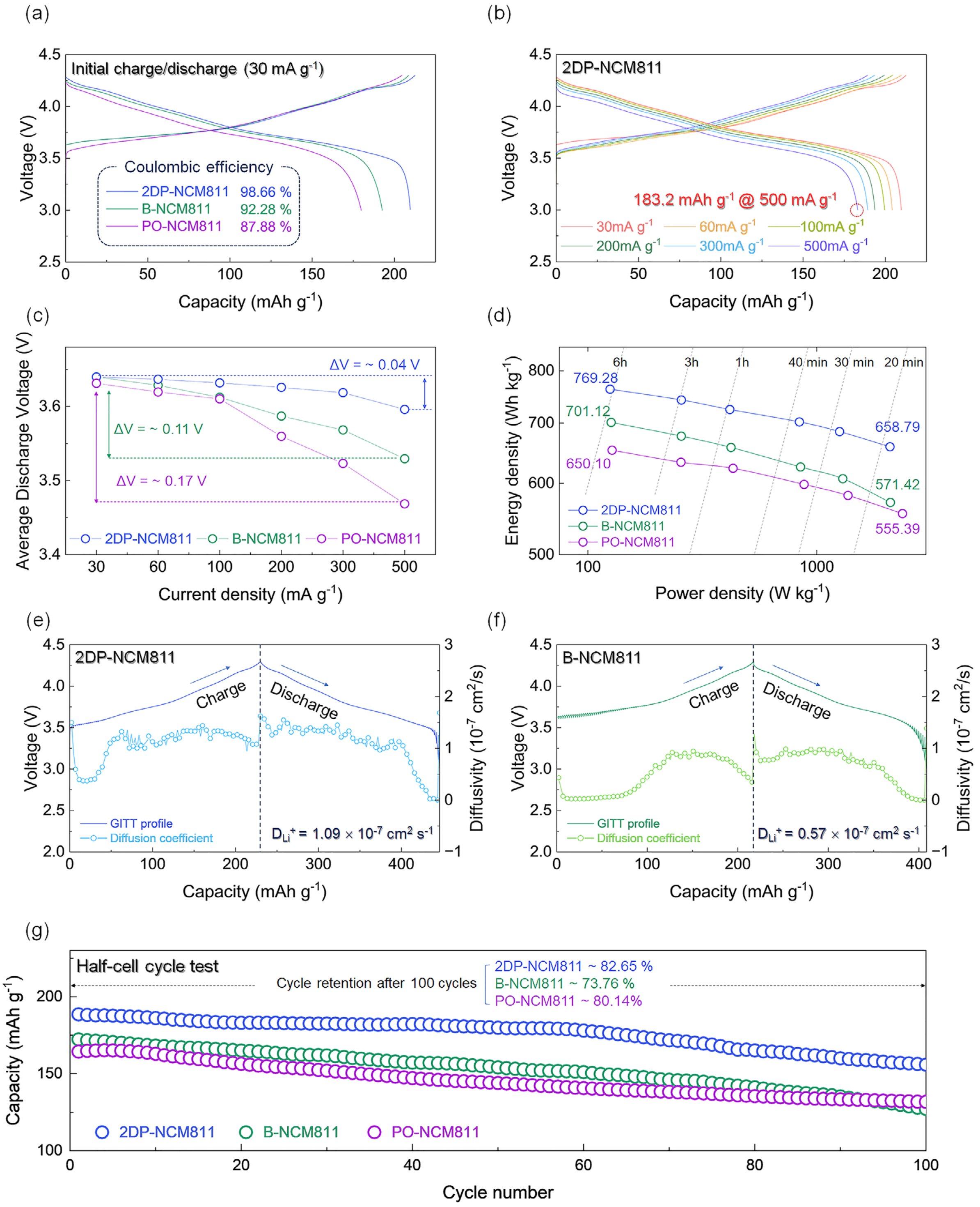

Figure 3. a) Initial charge–discharge profiles of the cathodes with a current density of 30 mA g^{-1}. b) Power capability of the 2DP-NCM811 cathode. c) Average discharge voltage of the cathodes at various current densities. d) Energy and power density of the cathodes. GITT test profiles and diffusion coefficient of e) 2DP-NCM811 and f) B-NCM811. g) Cyclability of the cathodes at a current density of 200 mA g^{-1} under the half-cell system.

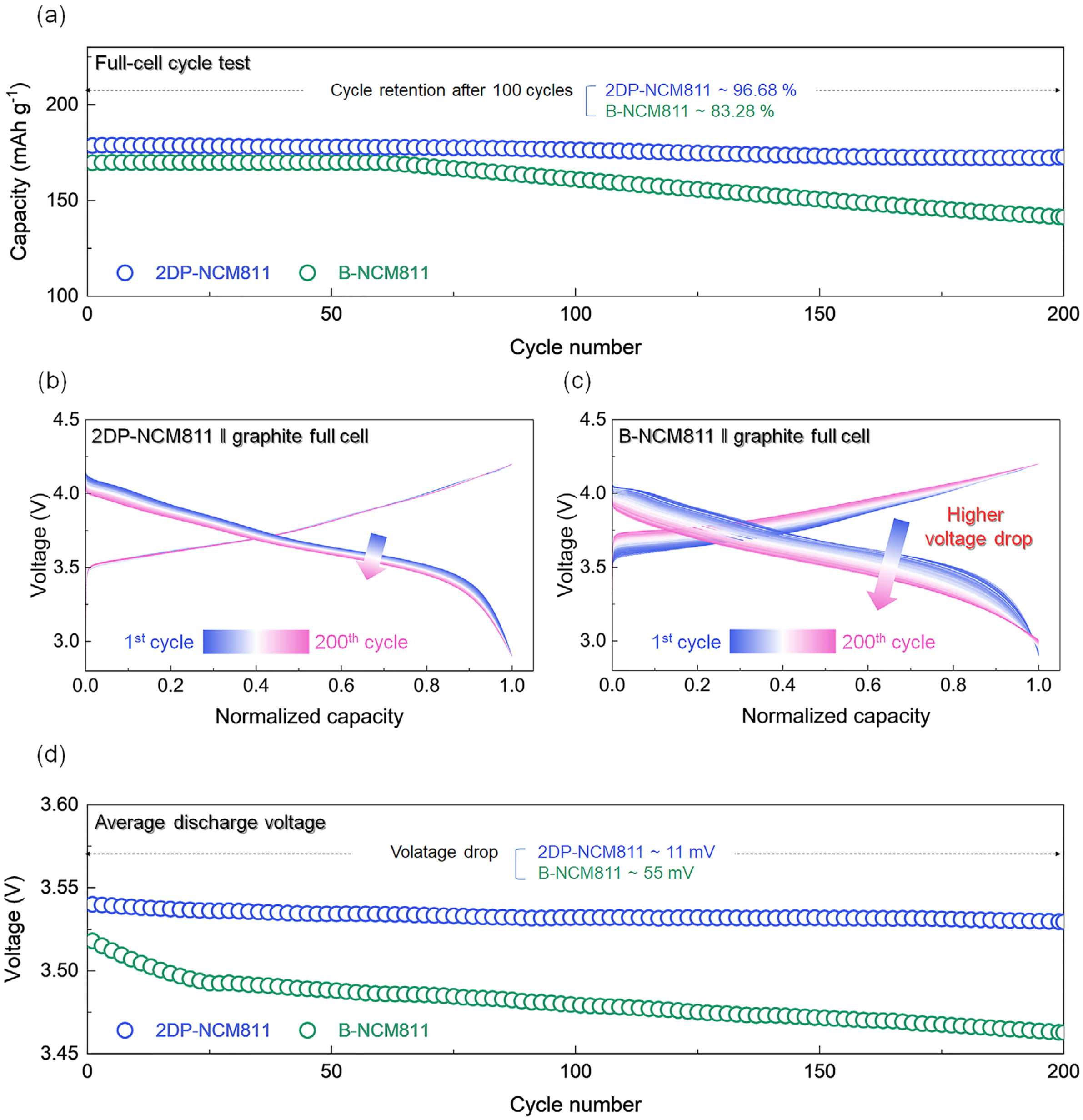

Figure 4. a) Cyclability of the cathodes at a current density of 200 mA g^{-1} under the full-cell system. Normalized charge–discharge profiles for b) the 2DP-NCM811||graphite full-cell and c) the B-NCM811||graphite full-cell. d) Average discharge voltage of the cathodes during the cycles under the full-cell system.

Under both conditions, 2DP-NCM811 still maintained relatively higher retention and discharge capacity than B-NCM811 and PO-NCM811. This result confirms that 2DP-NCM811 offers superior performance under both elevated temperature and high-voltage stress due to its ability to suppress interface degradation and ensure stable conductivity.

The enhanced cyclability of NCM811 by the 2DP-decorated coating was more clearly confirmed through the full-cell-based tests using a graphite anode. As shown in **Figure** 4a, it was verified that the 2DP-NCM811||graphite full-cell delivered the capacity retention of ≈96.68% after 200 cycles, while the capacity retention of the B-NCM811||graphite full-cell was just ≈83.28% retention at the same conditions.

Furthermore, the normalized Ch/Dis profiles of the two cathodes offered a comprehensive perspective on the differences in cycling performance by illustrating the evolution of cell polarization over repeated cycles (Figure 4b,c). Specifically, in the case of the B-NCM811||graphite full-cell, a continuous and pronounced decline in normalized capacity was observed throughout the Ch/Dis process up to 200 cycles. Conversely, the 2DP-NCM811||graphite full-cell exhibited lower polarization compared to the B-NCM811||graphite full-cell, with only minimal capacity fading.

This reduced polarization and improved capacity retention are further supported by the voltage decay analysis, which reveals that the 2DP-NCM811||graphite full-cell exhibited a voltage drop of ≈11 mV after 200 cycles-significantly lower than that of the B-NCM811||graphite full-cell (Figure 4d). These results indicate that uniform and thin 2DP-decorated coating effectively shields the NCM811 particles from undesirable side reactions degradation during prolonged cycling, leading to enhanced cyclability and fast Ch/Dis performance. Especially, when compared with other reported conductive coatings applied to NCM811 cathodes (Table S3, Supporting Information), the 2DP-NCM811 electrode in this work demonstrates superior capacity retention and rate performance under practical electrode conditions, highlighting its potential as a high-performance cathode material for next-generation LIBs.[46–52]

2.4. Structural and Morphological Changes of 2D Phosphorene Nanosheets (2DP)-Decorated NCM811 Cathode (2DP-NCM811)

To confirm the enhanced structural stability of 2DP-NCM811, we performed *operando* XRD analyses. As shown in **Figure** 5a,b, it was verified that both 2DP-NCM811 and B-NCM811 experienced the structural change, including H2-H3 phase transitions as a function of the state of charge (SOC), consistent with previous studies.[53,54]

Specifically, a shift in the (003) peak toward lower angles during charging up to 4.1 V (vs Li^+/Li) indicates an expansion of the *c*-lattice and an increase in interlayer spacing by O-O repulsion. Upon further charging to 4.3 V (vs Li^+/Li), the H2-H3 phase transition occurs, marked by a pronounced contraction of the *c*-lattice, resulting in the (003) peak shifting to higher 2θ angles.

Importantly, during the H2-H3 transition, the angular shift of the (003) peak was smaller for the 2DP-NCM811 ($\Delta 2\theta = 0.15°$) compared to the B-NCM811 ($\Delta 2\theta = 0.22°$), despite both having nearly identical SOCs (Figure 5c). Furthermore, Rietveld refinement of the *operando* XRD data (Figure 5d) revealed the overall lattice parameter changes in the NCM811 cathode during cycling.

For the 2DP-NCM811, the changes in the *a*- and *c*-lattice parameters were ≈2.16% and 2.82%, respectively, whereas the B-NCM811 showed larger variations of ≈2.3% and 3.31%. These findings demonstrate that the 2DP-decorated coating plays a critical role in reducing the structural evolution of the NCM811 cathode, thus contributing to enhanced cycle-performance.

To further validate these observations and gain deeper insight into the differences in lattice evolution between the B-NCM811 and 2DP-NCM811 cathodes during cycling, the lattice microstrain was quantitatively analyzed using the Williamson–Hall isotropic strain model (W-HISM).[55,56] The full width at half maximum (FWHM) of each X-ray diffraction peak was corrected for instrumental broadening effects, which were determined using lanthanum hexaboride (LaB_6) as a standard reference material.

This correction was performed according to Equation (2), where β_{hkl}, $\beta_{measured}$, and $\beta_{instrumental}$ represent the corrected, measured, and instrumental peak widths, respectively, expressed in radians.

$$\beta_{hkl} = \sqrt{\beta^2_{\text{measured}} - \beta^2_{instrumental}} \tag{2}$$

Within the W-HISM framework, the corrected β_{hkl} accounts for both lattice strain and crystallite size effects. To distinguish between these two contributions, the total peak broadening, which reflects the isotropic nature of the crystallites, was analyzed using Equation (3). In this equation, θ_{hkl} is the Bragg angle, D is the crystallite size, λ is the X-ray wavelength, and the shape factor K was set to 0.9.

$$\beta_{hkl}\ \cos\theta_{hkl} = 4\varepsilon \sin\theta_{hkl} + \frac{K\lambda}{D} \tag{3}$$

Based on the linear fitting of $\beta_{hkl}\cos\theta_{hkl}$ versus $4\sin\theta_{hkl}$, the calculated lattice strain (ε) values are calculated. As shown in Figures S16 and S17 (Supporting Information), the B-NCM811 cathode exhibited an increase in lattice strain of ≈32.94% compared to its pristine state, indicating significant structural degradation. In contrast, the 2DP-NCM811 cathode showed a marginal increase in lattice strain of ≈24.20%, suggesting that the 2DP-decorated coating effectively enhances the structural stability of the NCM811 cathode material during cycling.

The enhanced structural stability of NCM811 by the 2DP-decorated coating is also confirmed through comparison of the dQ/dV results. As shown in Figure 5e,f, dQ/dV curve in B-NCM811 was significantly changed as the cycles were processed, while that in 2DP-NCM811 was relatively well-retained after cycling.

Distinct differences were observed in the voltage regions at 3.7–4.0 V, indicative of the monoclinic phase, between B-NCM811 and 2DP-NCM811. While the presence of the monoclinic phase on B-NCM811 was challenging to confirm in the dQ/dV curve, it remained evident in the case of the 2DP-NCM811.[57]

In addition, we conducted ex situ HRTEM analyses to confirm the enhanced structural stability of NCM811 by the 2DP-decorated coating. As shown in Figure 5g,h, and B-NCM811 experienced noticeable structural degradation, leading to the formation of the rocksalt structure across a substantial surface area. This observation suggests the structural instability of the B-NCM811 during cycling. Conversely, the layered structure was significantly observed in the surface area of 2DP-NCM811 even after 100 cycles, indicating the restrained structural change in NCM811 by the 2DP-decorated coating.

We also compared the structural changes after cycling. As shown in Figure S18 (Supporting Information), it was verified that B-NCM811 showed a large shift of XRD peaks on (101) and (104) planes, while the XRD pattern of 2DP-NCM811 was well-retained with negligible changes. Especially, in comparison to 2DP-NCM811, B-NCM811 exhibited a significant decrease in the intensities of the peaks on the (101) and (104) planes. The XRD peak on the (101) plane of B-NCM811 showed a reduction of 16.96%, while that on the (104) plane decreased by 14.91%. In contrast, the XRD peak of the (101) plane on 2DP-NCM811 decreased by 10%, and the peak on the (104) plane decreased by 9.18%. These results indicate that the 2DP-decorated coating can provide an effective protective layer on the surface of NCM811 particles, contributing to the maintenance of the crystal structure during prolonged cycling.

This structural stability is further supported by ex situ X-ray photoelectron spectroscopy (XPS) analysis after 100 cycles

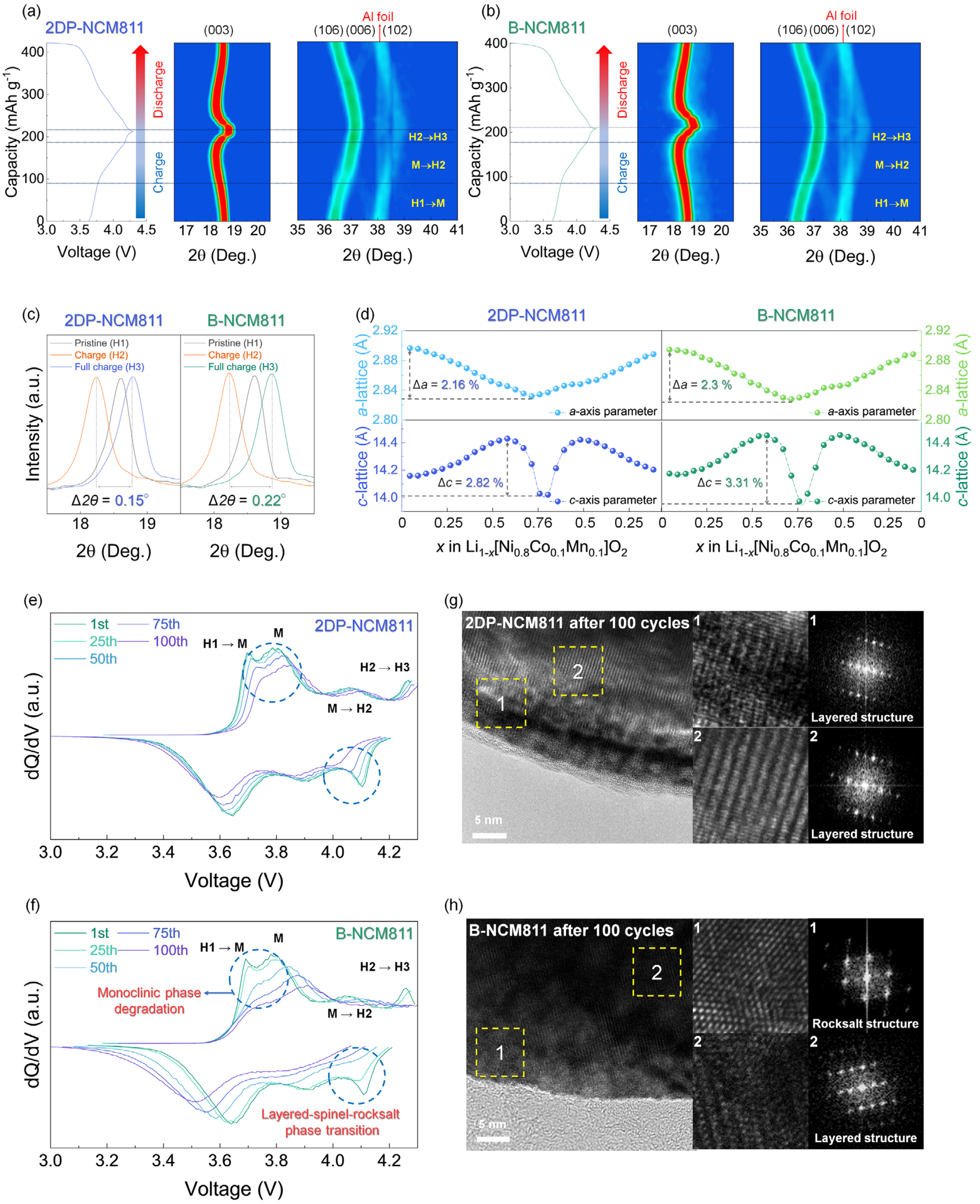

Figure 5. *Operando* XRD patterns of the a) 2DP-NCM811 and b) B-NCM811 cathode during charge–discharge. Comparison of the c) angular shift of the (003) peak and d) the overall lattice parameter changes based on *operando* XRD results. Comparison of dQ/dV curve and ex situ TEM images with their FFT images of the e,g) 2DP-NCM811 and f,h) B-NCM811 cathode after 100 cycles.

(Figure S19, Supporting Information). Compared to B-NCM811, which showed strong signals of Li_xPF_y and $Li_xF_yPO_z$ in both P 2p and F 1s spectra, indicating extensive electrolyte decomposition and CEI breakdown, 2DP-NCM811 exhibited notably weaker $Li_xF_yPO_z$ intensity.[58,59] This suggests that the 2DP-decorated coating effectively suppressed interfacial degradation reactions, consistent with prior reports on the protective role.[60,61] Moreover, Figure S20 (Supporting Information) shows a comparison of the morphology between B-NCM811 and 2DP-NCM811 after 100 cycles. B-NCM811 particles showed complete destruction after cycling, due to severe structural changes. 2DP-NCM811 particles, on the other hand, displayed well-preserved morphology after 100 cycles, which also supports the enhanced electrochemical performances of 2DP-NCM811.

3. Conclusion

In this study, we demonstrated that 2D phosphorene nanosheets (2DP), prepared via electrochemical exfoliation of black phosphorus (BP), can homogeneously wrap NCM811 particles with the aid of ethyl cellulose (EC), forming a conductive and uniform coating layer. This 2DP-based modification significantly improves both fast charge–discharge performance and cycling stability of Ni-rich NCM811 cathodes. Under practical conditions of high mass loading (18 mg cm^{-2}) and low carbon content (1 wt.%), the 2DP-decorated NCM811 (2DP-NCM811) delivered a high specific capacity of ≈209.7 mAh g^{-1} at a current density of 30 mA g^{-1}, outperforming bare NCM811 (192.6 mAh g^{-1}) and phosphate-modified NCM811 (179.9 mAh g^{-1}). At increased current densities, the gap in both capacity and average voltage became more pronounced, indicating enhanced rate capability of the 2DP-modified cathode. Furthermore, 2DP-NCM811 exhibited more stable long-term cycling, which correlated well with *operando* XRD and ex situ TEM results showing suppressed structural changes and surface degradation. This work offers an effective surface engineering strategy for improving both power and durability in Ni-rich layered cathodes under commercially relevant conditions. Leveraging the high conductivity, flexibility, and interfacial compatibility of 2DP, this work establishes a new surface design strategy that unifies charge transport enhancement and structural stabilization in Ni-rich layered cathodes for high-energy LIBs.

4. Experimental Section

Preparation of 2D Phosphorene Nanosheets (2DP) Solution: An electrochemical exfoliation cell was prepared by dissolving tetrabutylammonium bisulfate (0.1 M) in anhydrous acetonitrile, with a carbon electrode acting as the anode and a BP crystal clamped in a metallic clip serving as the cathode. Applying a constant potential of 6 V for 1 h drove the insertion of tetrabutylammonium ions (TBA$^+$) into the phosphorene layers, resulting in efficient exfoliation. Intercalants made the van der Waals force of each layer weaker, allowing the phosphorene crystal to be exfoliated only after a mild sonication process. The sonication process was performed for 1 h with poly(vinylpyrrolidone) (PVP) added dimethylformamide (DMF) solution. During sonication, PVP adsorbed onto the surface of black phosphorus nanosheets, providing steric stabilization that effectively suppressed restacking. After sonication, to obtain few-layer BP nanosheets, a centrifuge process was required. The dispersion was transferred to a conical tube, and the supernatant was collected after centrifuging at 2340 × g to remove unwanted bulk crystal. Typically, this process yielded ≈3 mL of 2DP dispersion at a concentration of 0.68 mg mL^{-1} from 50 mg of bulk BP crystal. Next step, to eliminate PVP and to change the solvent from DMF to isopropyl alcohol (IPA), the supernatant was collected and centrifuged at 2340 × g. The supernatant was replaced with IPA and redispersed with the sediments. This step is called the rinsing process, and rinsing will be repeated three times to clearly remove PVP and residue of DMF. Due to 2DP being vulnerable to oxidation, all processes were carried out under an Ar atmosphere using anhydrous solvents.

Preparation of Cathode Material: To fabricate 2DP-NCM811 cathode material, a desired amount of NCM811 was added to isopropanol, where 2DP and ethyl cellulose (EC) were dispersed. The 2DP-decorated coating on the surface of NCM811 was achieved by bath sonication for 20 min. To evaporate isopropanol, the solvent was dried using a vacuum oven at 80 °C for 3 h. The dried powder was calcined at 250 °C for 30 min under an Ar atmosphere. The processes for fabricating PO-NCM811 were carried out identically, with only the calcination step being conducted in an O_2 atmosphere for 5 h.

Materials Characterization: The crystal structures of 2DP-NCM811, B-NCM811, and PO-NCM811 were characterized using X-ray diffraction (XRD; PANalytical Empyrean) with Cu K-alpha radiation (λ = 1.54178 Å). Data were collected over a 2θ range of 10°–80° with a step size of 0.026°. The obtained XRD data were analyzed by Rietveld refinement using the FullProf software. *Operando* XRD patterns of the cathodes were recorded during charge and discharge at a current density of 30 mA g^{-1} within a voltage range of 3.0–4.3 V (vs Li$^+$/Li).

The morphology and elemental distribution were examined using field-emission scanning electron microscopy (FE-SEM; GeminiSEM 560) and energy-dispersive X-ray spectroscopy (EDS) mapping at the National Center for Inter-university Research Facilities (NCIRF), Seoul National University. Further morphological and microstructural analyses were conducted using field-emission transmission electron microscopy (FE-TEM; JEM-ARM200F) at the Advanced Facility Center for Quantum Technology (AQT), Sungkyunkwan University, and high-resolution transmission electron microscopy (HR-TEM; FEI TITAN 80–300) at the Korea Institute of Science and Technology (KIST). Raman spectroscopy was performed using the XperRAM 200 (NanoBase) at AQT, Sungkyunkwan University.

Electrochemical Characterization: The electrodes of the active materials were fabricated by mixing 97 wt.% of the active material, 1 wt.% of Super P carbon black, and 2 wt.% of polyvinylidene fluoride (PVDF) using N-methyl-2-pyrrolidone (NMP) as the solvent. The slurry was applied on Al foil using a doctor blade, and each electrode was dried in an oven at 100 °C for 12 h. CR2032 cells were fabricated as half-cells using the electrode (mass loading of cathode ≈18 mg cm^{-2}), Li metal as the counter electrode, a separator (Celgard 2400), and 1.15 M $LiPF_6$ in ethylene carbonate: ethyl methyl carbonate: dimethyl carbonate (volume ratio of 2:4:4) as the electrolyte in an Ar-filled glove box. The electrochemical performance was evaluated in the voltage range of 3.0–4.3 V at 30 °C using a battery test system (WonATech WBCS3000). Each full cell consisted of a 2DP-NCM811 or B-NCM811 cathode, a separator (Celgard 2400), an electrolyte of 1.15 M $LiPF_6$ in ethylene carbonate: ethyl methyl carbonate: dimethyl carbonate (volume ratio 2:4:4), and a graphite anode. The full-cell electrode was designed with an N/P ratio of 1.2.

Supporting Information

Supporting Information is available from the Wiley Online Library or from the author.

Acknowledgements

J.L. and K.N. contributed equally to this work. This work was supported by the National R&D Program through the National Research Foundation of Korea (NRF) funded by the Ministry of Science and ICT (RS 2024–00408156) of the Republic of Korea. This work was also supported by the NRF grant funded by the Minisitry of Science and ICT (RS-2023-00208538).

Conflict of Interest

The authors declare no conflict of interest.

Data Availability Statement

The data that support the findings of this study are available from the corresponding author upon reasonable request.

Keywords

cathode, conductive coating, high-Ni, Li-ion batteries, phosphorene

Received: May 7, 2025
Revised: July 29, 2025
Published online: August 25, 2025

---

[1] B. Li, Z. Zhuo, L. Zhang, A. Iadecola, X. Gao, J. Guo, W. Yang, A. V. Morozov, A. M. Abakumov, J. M. Tarascon, *Nat. Mater.* **2023**, *22*, 1370.
[2] J. Heo, S. K. Jung, I. Hwang, S. P. Cho, D. Eum, H. Park, J. H. Song, S. Yu, K. Oh, G. Kwon, T. Hwang, K. H. Ko, K. Kang, *Nat. Energy* **2023**, *8*, 30.
[3] M. Choi, H. B. Lee, Y. Lee, H. Kweon, J. Ahn, B. Ku, J. Lee, S. Lee, J. Park, Y. M. Kim, J. Kim, *Adv. Funct. Mater.* **2025**, *35*, 2424880.
[4] N. Kim, Y. Kim, J. Sung, J. Cho, *Nat. Energy* **2023**, *8*, 921.
[5] F. Degen, M. Winter, D. Bendig, J. Tübke, *Nat. Energy* **2023**, *8*, 1284.
[6] G. Lim, M. K. Cho, J. Choi, K. J. Zhou, D. Shin, S. Jeon, M. Kwon, A. R. Jeon, J. Choi, S. S. Sohn, M. Lee, J. Hong, *Energy Environ. Sci.* **2024**, *17*, 9623.
[7] S. Ko, X. Han, T. Shimada, N. Takenaka, Y. Yamada, A. Yamada, *Nat. Sustain.* **2023**, *6*, 1705.
[8] L. Yu, A. Dai, T. Zhou, W. Huang, J. Wang, T. Li, X. He, L. Ma, X. Xiao, M. Ge, R. Amine, S. N. Ehrlich, X. Ou, J. Wen, T. Liu, K. Amine, *Nat. Commun.* **2025**, *16*, 434.
[9] J. Kim, H. Ahn, J. Ahn, H. Park, J. Hong, M. Hwan Lee, H. Park, J. Kim, *Chem. Eng. J.* **2024**, *495*, 153122.
[10] H. Cheng, Z. Ma, P. Kumar, H. Liang, Z. Cao, H. Xie, L. Cavallo, H. Kim, Q. Li, Y. K. Sun, J. Ming, *Adv. Energy Mater.* **2024**, *9*, 1604.
[11] C. H. Chen, J. Liu, M. E. Stoll, G. Henriksen, D. R. Vissers, K. Amine, *J. Power Sources* **2004**, *128*, 278.
[12] C. Liu, Z. Cui, A. Manthiram, *Adv. Energy Mater.* **2024**, *14*, 2302722.
[13] H. J. Noh, S. Youn, C. S. Yoon, Y. K. Sun, *J. Power Sources* **2013**, *233*, 121.
[14] H. He, J. Dong, D. Zhang, D. Hang, X. Zhu, C. Chang, *Int. J. Energy Res.* **2021**, *45*, 7108.
[15] S. T. Myung, F. Maglia, K. J. Park, C. S. Yoon, P. Lamp, S. J. Kim, Y. K. Sun, *Am. Chem. Soc.* **2017**, *2*, 196.
[16] M. Dixit, B. Markovsky, F. Schipper, D. Aurbach, D. T. Major, *J. Phys. Chem. C* **2017**, *121*, 22628.
[17] C. S. Yoon, D. W. Jun, S. T. Myung, Y. K. Sun, *ACS Energy Lett.* **2017**, *2*, 1150.
[18] H. Kim, M. G. Kim, H. Y. Jeong, H. Nam, J. Cho, *Nano Lett.* **2015**, *15*, 2111.
[19] A. Rajkamal, H. Kim, *ACS Appl. Energy Mater.* **2021**, *4*, 14068.
[20] L. Wang, Q. Su, B. Han, W. Shi, G. Du, Y. Wang, H. Li, L. Gu, W. Zhao, S. Ding, M. Zhang, Y. Yang, B. Xu, *J. Energy Chem.* **2023**, *77*, 428.
[21] X. Kong, H. Yang, Y. Zhang, P. Dai, Y. Tang, J. Zeng, J. Zhao, *Chem. Eng. J.* **2023**, *452*, 139431.
[22] Y. Kim, H. S. Kim, S. W. Martin, *Electrochim. Acta* **2006**, *52*, 1316.
[23] M. K. Azar, M. A. Razmjoo Khollari, M. Esmaeili, E. Heidari, S. M. Hosseini-Hosseinabad, R. Siavash Moakhar, A. Dolati, S. Ramakrishna, *ACS Appl. Energy Mater.* **2021**, *4*, 934.
[24] H. Zhang, H. Zhao, J. Xu, J. Zhang, *Int. J. Green Energy* **2020**, *17*, 447.
[25] H. Liang, J. Chen, L. Li, Y. Fu, J. Wang, X. Huang, X. Hu, G. Zhou, *Ionics* **2025**, *31*, 4121.
[26] B.-S. Lee, Z. Wu, V. Petrova, X. Xing, H.-D. Lim, H. Liu, P. Liu, *J. Electrochem. Soc.* **2018**, *165*, A525.
[27] S. Liu, H. Wu, L. Huang, M. Xiang, H. Liu, Y. Zhang, *J. Alloys Compd.* **2016**, *674*, 447.
[28] L. Li, Y. Yu, G. J. Ye, Q. Ge, X. Ou, H. Wu, D. Feng, X. H. Chen, Y. Zhang, *Nat. Nanotechnol.* **2014**, *9*, 372.
[29] J. Sun, H. W. Lee, M. Pasta, H. Yuan, G. Zheng, Y. Sun, Y. Li, Y. Cui, *Nat. Nanotechnol.* **2015**, *10*, 980.
[30] Q. Wei, X. Peng, *Appl. Phys. Lett.* **2014**, *104*, 251915.
[31] F. B. Phosphorus, J. Tao, W. Shen, S. Wu, L. Liu, Z. Feng, C. Wang, C. Hu, P. Yao, *ACS Nano* **2015**, *9*, 11362.
[32] J. Qiao, X. Kong, Z. X. Hu, F. Yang, W. Ji, *Nat. Commun.* **2014**, *5*, 4475.
[33] H. Liu, A. T. Neal, Z. Zhu, Z. Luo, X. Xu, D. Tománek, P. D. Ye, *ACS Nano* **2014**, *8*, 4033.
[34] J. Kang, J. D. Wood, S. A. Wells, J. H. Lee, X. Liu, K. S. Chen, M. C. Hersam, *ACS Nano* **2015**, *9*, 3596.
[35] J. Kang, S. A. Wells, J. D. Wood, J. H. Lee, X. Liu, C. R. Ryder, J. Zhu, J. R. Guest, C. A. Husko, M. C. Hersam, *Proc. Natl. Acad. Sci. USA* **2016**, *113*, 11688.
[36] J. Kang, S. A. Wells, V. K. Sangwan, D. Lam, X. Liu, J. Luxa, Z. Sofer, M. C. Hersam, *Adv. Mater.* **2018**, *30*, 1706102.
[37] Y. Jeon, D. Rhee, B. Wu, V. Mazanek, I. S. Kim, D. Son, Z. Sofer, J. Kang, *npj 2D Mater. Appl.* **2022**, *6*, 82.
[38] Z. Lin, Y. Huang, X. Duan, *Nature Research* **2019**, *2*, 378.
[39] S. Kim, J. Kim, J. Kang, W. H. Ryu, *npj 2D Mater. Appl.* **2025**, *9*, 14.
[40] S. Rehman, M. F. Khan, S. Aftab, H. Kim, J. Eom, D. K. Kim, *J. Mater. Chem. C* **2019**, *7*, 725.
[41] J. Sun, G. Zheng, H. W. Lee, N. Liu, H. Wang, H. Yao, W. Yang, Y. Cui, *Nano Lett.* **2014**, *14*, 4573.
[42] W. Kong, H. Wang, L. Sun, C. Su, X. Liu, *Appl. Surf. Sci.* **2019**, *497*, 143814.
[43] X. Wang, Y. Song, H. Cui, J. Liu, H. Huo, L. Wang, Y. Gao, X. He, *Energy Environ. Mater.* **2023**, *6*, 1.
[44] W. Li, X. Liu, Q. Xie, Y. You, M. Chi, A. Manthiram, *Chem. Mater.* **2020**, *32*, 7796.
[45] Y. Zhang, C. Yin, B. Qiu, G. Chen, Y. Shang, Z. Liu, *Energy Storage Mater.* **2022**, *53*, 763.
[46] S. She, Y. Zhou, Z. Hong, Y. Huang, Y. Wu, *ACS Omega* **2022**, *7*, 24851.
[47] Q. Fan, S. Yang, J. Liu, H. Liu, K. Lin, R. Liu, C. Hong, L. Liu, Y. Chen, K. An, P. Liu, Z. Shi, Y. Yang, *J. Power Sources* **2019**, *421*, 91.
[48] B. Zhou, Y. Qi, Y. Zhang, Z. Wang, P. Wei, K. Liang, J. Li, Y. Ren, *Appl. Surf. Sci.* **2023**, *631*, 157449.
[49] M. Wang, X. Zhang, Z. Guo, C. Chen, J. Yuan, Y. Li, Y. Xia, Y. J. Cheng, *Electrochim. Acta* **2023**, *454*, 142339.
[50] G. Zha, N. Hu, Y. Luo, X. Fu, H. Jin, L. Li, Q. Huang, C. Ouyang, H. Hou, *Electrochim. Acta* **2023**, *451*, 142284.
[51] W. Zhang, L. Liang, F. Zhao, Y. Liu, L. Hou, C. Yuan, *Electrochim. Acta* **2020**, *340*, 1.
[52] Z. Chen, Q. Zhang, W. Tang, D. Li, J. Ding, C. Huang, Z. Yang, W. Zhang, G. Wu, H. Chen, *ACS Appl. Energy Mater.* **2021**, *4*, 13785.
[53] S. K. Jung, H. Kim, S. H. Song, S. Lee, J. Kim, K. Kang, *Adv. Funct. Mater.* **2022**, *32*, 1.
[54] G. Xu, Q. Liu, K. K. S. Lau, Y. Liu, X. Liu, H. Gao, X. Zhou, M. Zhuang, Y. Ren, J. Li, M. Shao, M. Ouyang, F. Pan, Z. Chen, K. Amine, G. Chen, *Nat. Energy* **2019**, 4.
[55] P. M. Shafi, A. C. Bose, *A. I. P. Adv.* **2015**, *5*, 057137.
[56] K. Venkateswarlu, A. Chandra Bose, N. Rameshbabu, *Phys. B Condens. Matter* **2010**, *405*, 4256.

[57] J. Yang, Y. Xia, *ACS Appl. Mater. Interfaces* **2016**, *8*, 1297.
[58] R. Jung, M. Metzger, F. Maglia, C. Stinner, H. A. Gasteiger, *J. Phys. Chem. Lett.* **2017**, *8*, 4820.
[59] W. Zhao, K. Wang, R. Dubey, F. Ren, E. Brack, M. Becker, R. Grissa, L. Seidl, F. Pagani, K. Egorov, K. V. Kravchyk, M. V. Kovalenko, P. Yan, Y. Yang, C. Battaglia, *Mater. Today Energy* **2023**, *34*, 101301.
[60] Z. Chen, H. D. Nguyen, M. Zarrabeitia, H. P. Liang, D. Geiger, J. K. Kim, U. Kaiser, S. Passerini, C. Iojoiu, D. Bresser, *Adv. Funct. Mater.* **2021**, *31*, 1.
[61] Y. Li, L. Cui, C. Tan, X. Fan, Q. Pan, Y. Chu, S. Hu, F. Zheng, H. Wang, Q. Li, *Chem. Eng. J.* **2022**, *430*, 132985.